

# X-Ray-Absorption Fine-Structure Spectroscopy Study of the Interactions between Contaminant Tetrahedral Anions and Self-Assembled Monolayers on Mesoporous Supports

S. D. Kelly\* and K. M. Kemner

Bldg 203, Rm E-113, Argonne National Laboratory, Argonne, Illinois 60439

G. E. Fryxell, J. Liu, S. V. Mattigod, and K. F. Ferris

Pacific Northwest National Laboratory, Richland, Washington 99352

Received: December 31, 2000; In Final Form: April 21, 2001

Self-assembled monolayers on mesoporous supports (SAMMSs) have been found to be superior sorbent materials for sequestering environmentally problematic species. Coupling the rich coordination chemistry of transition metal complexes with the SAMMS concept has afforded anion-specific sorbent materials with unprecedented anion binding capabilities. X-ray-absorption fine-structure (XAFS) spectroscopy is used to investigate the chemical interaction between an interfacially bound copper ethylenediamine complex (Cu(EDA)) and arsenate and chromate anions within these nanoporous hybrid materials. The Cu K-edge XAFS data indicate a structural change of Cu(EDA)<sub>3</sub> caused by the anion bonding, consistent with a lock-and-key mechanism. The As and Cr K-edge features of the normalized absorption data signify As(V) and Cr(VI) in the SAMMS samples. The Cr K-edge data show a distorted CrO<sub>4</sub> tetrahedron with two short and two long oxygen distances, whereas the AsO<sub>4</sub> tetrahedron is symmetric. The average local structure about Cu, As, and Cr consistently indicate direct Cu–O bond formation, a monodentate linkage between the anion and the Cu(II) cation, and a trigonal bipyramidal geometry of the Cu center in the adduct.

## I. Introduction: Waste Management and SAMMSs

Arsenic and chromium are listed as priority pollutants with the U.S. Environmental Protection Agencies. Groundwater contamination by geologic arsenic has recently become of great concern in many parts of the world, such as Bangladesh,<sup>1</sup> New England,<sup>2</sup> and California.<sup>3</sup> The use of arsenic and chromium in an array of agricultural and industrial processes has also resulted in groundwater contamination of many industrial sites (e.g., Puget Sound).<sup>4</sup> These situations have created the need for the development of effective groundwater remediation strategies for the selective removal of these oxometalate anions. Unfortunately, most anion exchange methods are centered around some sort of quaternary ammonium (or phosphonium) salt and have little, if any, interaction between the cation/anion pair, and thus, selectivity is modest at best. In a complex groundwater matrix, which contains many ubiquitous anions (e.g., sulfate) that are present at considerably higher concentrations than that of the target oxometalate, this lack of selectivity constitutes a fatal flaw for existing anion exchange methods.

The need also exists in the management of DOE's high level wastes (HLW) to be able to selectively and completely remove the radionuclide components so that HLW volume can be minimized and the nonradioactive components can be segregated and disposed of as low-level waste. A key component of this need is a complete and accurate accounting of Tc-99 concentration and speciation, since Tc-99 dominates the radionuclide dose after closure and is therefore critical information for waste vitrification vendors. An improved methodology for binding the pertechnetate anion would help address this need, as well as improve radiochemical analysis of high ionic strength samples

by separating the Tc-99 from the problematic matrix. Chromate can be used as a nonradioactive model system with which to study pertechnetate binding. In addition, DOE has a significant need for so-called "getter materials" (sorbent barrier materials), especially for anionic targets. Anions are poorly sorbed onto most materials under alkaline conditions. If anionic getter materials can be developed, this could save hundreds of millions of dollars in the DOE cleanup. There is a wide variety of anionic targets for better materials, including pertechnetate, iodide, selenate, niobate, chromate, etc.

In recent years, self-assembled monolayers on mesoporous supports (SAMMSs) have been found to be superior sorbent materials for the sequestration of heavy metal cations (e.g., Hg<sup>2+</sup>, Cd<sup>2+</sup>, Ag<sup>+</sup>, Cu<sup>2+</sup>, etc.).<sup>5–13</sup> The SAMMSs concept allows for significant freedom in the design and synthesis of tailored materials for separations. The mesoporous ceramic synthesis is quite general and can be used to prepare a variety of high surface area ceramic oxide supports that are stable in different environments (acidic, corrosive, oxidizing, etc.). The high surface area of the mesoporous support (ca. 1000 m<sup>2</sup>/g), coupled with the high population density of binding groups, creates a high loading capacity in the final SAMMSs material. Molecular self-assembly provides for the direct introduction of a variety of useful chemical interfaces, and subsequent synthetic elaboration of this monolayer foundation allows for virtually unlimited interfacial design.

Unlike the previously mentioned heavy metal contaminants, arsenic, chromium, and technetium are commonly present as oxometalate anions (e.g., chromate, arsenate, and pertechnetate). The development of anion-specific separation techniques and novel materials has been complicated by the fact that many anions of concern are similar in size and coordination geometry.

\* Corresponding author. E-mail: skelly@anl.gov.

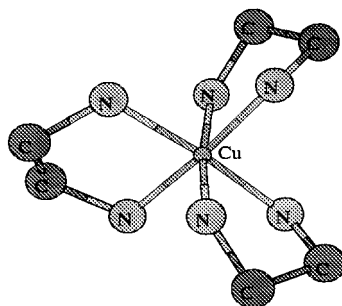


**Figure 1.** Suggested structure of Cu in the SAMMS. The octahedral complex formed from three EDA ligands about a Cu(II) ion. Each C or N has two closely bound H atoms, which are left out of the figure for simplicity.

Recently, the synthesis of SAMMSs lined with cationic metal complexes as a novel anion binding material was reported in ref 14. It has been demonstrated that these metalated SAMMSs materials (incorporating a monolayer of ethylenediamine (EDA) ligands bound to the mesoporous silica with three EDA ligands chelated to a central Cu(II) ion) can very effectively remove arsenate and chromate in the presence of comparatively high concentrations of other anions (such as sulfate) from solutions containing typical groundwater concentrations of the toxic oxometalate anions.

To understand the interfacial chemistry of these cationic SAMMSs, both to evaluate them as anion sorbent materials and to look at the long-term stability of them as potential waste forms, it is critical that we understand not only how well the anion is associated with the metal complex, but also how well the metal complex remains anchored within the mesoporous support. Is the anion sorbed through simple anion metathesis, or is it directly bound to the metal cation? If bound, is it bound in a monodentate, bidentate, or bridging fashion? Is the anion displaceable or fixed in place? What effect does anion binding have on the stereochemistry and geometry of the metal complex, and what does this stereochemical information reveal about the long-term chemical stability (leachability) of the adduct? In an effort to answer these questions, we have undertaken a detailed study of the local atomic environment around the metal complex, both before and after the oxometalate anions have been bound to the SAMMSs interface. This stereochemical insight is critical for the development of selective anion-specific sorbent materials. XAFS spectroscopy is a direct probe of the average local atomic environment about a specific atomic species.<sup>15,16</sup> Theoretical XAFS calculations using FEFF7 software<sup>17</sup> indicate that mono-, bi-, and tridentate bonding between the toxic oxyanions and the SAMMSs can be distinguished on the basis of the distance between the Cu(II) ion in the end member of the SAMMSs and the As/Cr/S atom of the oxyanion. XAFS measurements of the SAMMS and a variety of standards are made at the Cu, As, and Cr K-edges to determine the average local structure about the Cu, As, and Cr atoms, respectively. The results of these studies are summarized in this manuscript.

## II. XAFS Experiment

A complete description of the synthesis of the SAMMS samples is in ref 4. Four SAMMSs samples were investigated in this study. Each of these samples consisted of Cu(II) ions bound to ethylenediamine (EDA) ligands, contained within the monolayer on the mesoporous silica. The Cu(II) ions are thought to form an octahedral complex from three EDA ligands, as shown in Figure 1. This octahedral complex provides ideal binding sites for tetrahedral anions. Because  $\text{SO}_4$  is present with

$\text{AsO}_4$  and  $\text{CrO}_4$  in DOE waste tanks, the SAMMSs samples were designed to have increased affinity for  $\text{AsO}_4$  and  $\text{CrO}_4$ , as compared to the affinity for  $\text{SO}_4$ . The SAMMSs samples investigated in this work are designated SAMMS (indicating that no anion was introduced to the SAMMSs), SAMMS +  $\text{SO}_4$  (indicating that  $\text{SO}_4$  was introduced to the SAMMSs), SAMMS +  $\text{SO}_4/\text{CrO}_4$  (indicating that a 1:4 mixture  $\text{SO}_4$  and  $\text{CrO}_4$  was introduced to the SAMMSs), and SAMMS +  $\text{SO}_4/\text{AsO}_4$  (indicating that a 1:4 mixture of  $\text{SO}_4$  and  $\text{AsO}_4$  was introduced to the SAMMSs).

The transmission XAFS data were collected at the Materials Research Collaborative Access Team (MR-CAT) sector<sup>18</sup> at the Advanced Photon Source (APS) on the SAMMS sample and at the National Institutes and Technology beamline X23A2 at the National Synchrotron Light Source (NSLS) on the remaining samples. Cu K-edge data were collected for each of these samples at  $\sim 100$  K and for the SAMMS +  $\text{SO}_4$  sample at room temperature. Cr K-edge data were collected for the SAMMS +  $\text{CrO}_4/\text{SO}_4$  sample at room temperature, and As K-edge data were collected for the SAMMS +  $\text{AsO}_4/\text{SO}_4$  sample at  $\sim 100$  K and at room temperature.

The fine-grained powder samples were packed in Kapton tape and mounted in a displax or a liquid-nitrogen-cooled coldfinger for the  $\sim 100$  K measurements made at MR-CAT or X23A2, respectively.

For the experiments performed at the bending-magnet X23A2 beamline, a fixed-exit double-crystal silicon [220] monochromator was used to select the X-ray energy. The appropriate gas or gas mixture was used to achieve 10–15% absorption in the incident X-ray ion chamber, and argon gas was used in the transmission ion chamber. For the experiments performed at MR-CAT, the undulator gap was tapered ( $\Delta E = 200$  eV) and scanned while a double-crystal silicon [111] monochromator was used to select the X-ray energy. Higher-order harmonics were removed with a harmonic rejection mirror. The incident ion gas chamber was filled with a nitrogen/helium (10/90) mixture, and the transmission ion chamber was filled with argon. Linearity tests<sup>19</sup> were performed on each sample before the data were collected. The results indicate less than 0.5% nonlinearity in the experimental setup for 50% attenuation of the incoming X-ray beam intensity. All of the measurements were made at least twice, and the resulting  $\chi(k)$  data were averaged.

## III. Data Analysis

The analysis software is part of the UWXAFS package.<sup>20</sup> These programs include AUTOBK<sup>21</sup> for background removal, FEFF7<sup>17</sup> for generation of the theoretical models, and FEFFIT<sup>22</sup> for parameter optimization of the model. A brief description of the analysis procedure used is given below.

**A. Energy Alignment, Background Removal, and Fourier Transform.** The absorption value is the log of the ratio of the measured transmitted to incident X-ray intensities as a function of X-ray energy. The pre-edge background was removed, and the data were normalized to a step height of 1.0. This is done so that  $E_0$ , the Fermi energy, can be consistently chosen at the middle of the edge step for all data sets (see Figure 2a).  $E_0$  is used by AUTOBK to determine the photoelectron wavenumber:  $k = \sqrt{2m(E - E_0)/\hbar^2}$ , where  $m$  is the electron mass,  $\hbar$  is Planck's constant, and  $E$  is the incident X-ray energy. By using this equation, we converted the measured XAFS [ $\chi(E)$ ] data to  $\chi(k)$  data.

The background function generated by AUTOBK is made from several third-order splines connected by knots. An example of a background function is shown in Figure 2a. The number

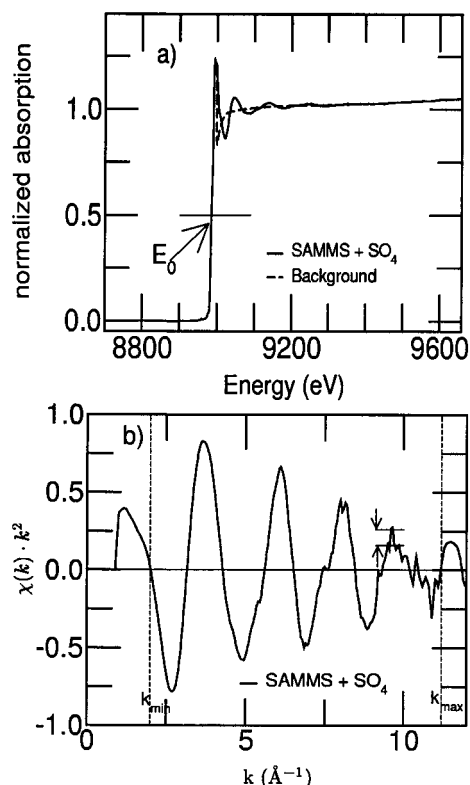


**Figure 2.** Cu K-edge data from the SAMMS + SO<sub>4</sub> sample at ~100 K. (a) Normalized absorption data and background function. The arrow indicates the value for  $E_0$ . (b) Background-subtracted  $\chi(k)k^2$  data. The vertical lines represent the data range used in the Fourier transform. The amplitude between the horizontal lines, indicated by arrows, corresponds to 0.07 noise in the data.

of knots, determined by the energy range of the data and by an input parameter  $R_{\text{bkg}}$ , sets a high-frequency limit on the background.  $R_{\text{bkg}}$  is chosen so that the correlation between the fitted parameters and the background is less than 50%. The  $R_{\text{bkg}}$  value is in reference to the Fourier transform of the  $\chi(k)$  data and is related to the distance between the excited atom and its neighbors.

The statistical error in the  $\chi(k) \cdot k^2$  data can be estimated easily. The amplitude between the horizontal lines, marked by arrows in Figure 2b, indicates that the peak-to-peak noise at 10 Å<sup>-1</sup> is approximately 0.1. Because the data are scaled by a multiplicative value of  $k^2$ , the actual peak-to-peak noise at 10 Å<sup>-1</sup> is 0.001. Division of this value by  $\sqrt{2}$  determines a maximum mean-square noise value of 0.07. In general, a statistical error of approximately 0.1 is considered to be the limit of detection. Thus, the data for this analysis are of very high quality.

The magnitude and real part of the Fourier transform of the  $\chi(k)$  data ( $|\tilde{\chi}(R)|$  and  $\text{Re}\tilde{\chi}(R)$ , respectively) are shown in Figure 3a. The Fourier transform parameters used in the analysis are listed in Table 1. The positions of the peaks in the Fourier transform are related to the distance between the absorbing atoms and the neighboring atoms, and the height is related to the number of neighboring atoms at this distance.

**B. Theoretical Models.** A trial structure is given as input to the FEFF7 code to generate a theoretical model. The theoretical models are written as a sum of paths of the photoelectron. A path is the contribution to the XAFS data by a component of the photoelectron that travels from the absorbing atom and then is scattered from one or more neighboring atoms and finally returns to the absorbing atom. Each path has several adjustable parameters optimized by FEFFIT to fit the data. These parameters include the passive electron reduction factor ( $S_0^2$ ),

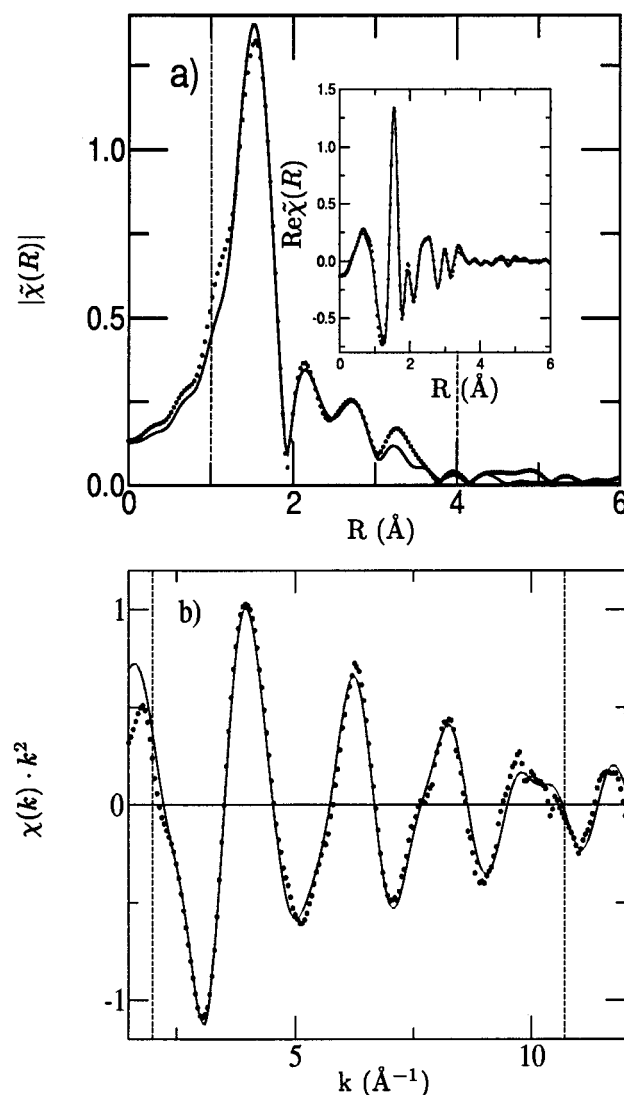


**Figure 3.** Cu K-edge data from the SAMMS + SO<sub>4</sub> sample and the model. The dashed vertical lines represent the fit range. (a) The magnitude of the Fourier transform. (inset) The real part of the Fourier transform. (b) Nonfiltered  $\chi(k)k^2$  data and model.

**TABLE 1: Fourier Transform Parameters, along with the Fit and Data Ranges for Each SAMMS Sample<sup>a</sup>**

K-edge	sample	$R$ -range (Å)	$k$ -range (Å <sup>-1</sup> )
Cu	SAMMS + SO <sub>4</sub>	[1.0:4.0]	[2.0:10.7]
Cu	SAMMS + SO <sub>4</sub> /AsO <sub>4</sub>	[1.0:4.0]	[2.0:10.7]
Cu	SAMMS + SO <sub>4</sub> /CrO <sub>4</sub>	[1.0:4.0]	[2.0:10.7]
Cu	SAMMS	[1.0:3.5]	[3.2:11.0]
As	SAMMS + SO <sub>4</sub> /AsO <sub>4</sub>	[1.0:4.0]	[2.7:12.6]
Cr	SAMMS + SO <sub>4</sub> /CrO <sub>4</sub>	[1.0:4.0]	[2.5:11.0]

<sup>a</sup> The fit range is specified in  $R$ -space, the data range that was Fourier transformed in  $k$ -space. The Fourier transform parameters include  $dk = 2.0$ , the full width of the sill, and a  $k$ -weighting of 1, 2, or 3. A Hanning window was used in each Fourier transform.

the number of identical paths ( $N_{\text{degen}}$ ), the relative mean-square displacement of the atoms included in path  $i$  ( $\sigma_i^2$ ), an energy shift for each path<sup>23</sup> ( $\Delta E_{0i}$ ), and a change in the path length ( $\Delta R_i$ ). Several of our models include as many as 15 paths, and therefore, several constraints were used to reduce the number of fit parameters. These constraints are discussed in detail in the section that describes each model.

**C. Debye Model.** The correlated Debye model<sup>24</sup> is used in the analysis of the data to reduce the number of fit parameters.



Using the correlated Debye model with a single Debye temperature for all paths containing C, N, and/or O scattering atoms, which are very similar in mass and size, is less restrictive than constraining the paths to have the same  $\sigma_i^2$  value and uses far fewer parameters than allowing each path to have an independent  $\sigma_i^2$  value. Within this model, the correlated Debye temperature, along with the atom types and the path length, determines the value for  $\sigma_i^2$ .

**D. Goodness-of-Fit Values.** A detailed discussion of the goodness-of-fit values can be found in ref 12. Because these definitions are not standard for all XAFS analyses, the following is a brief discussion of the goodness-of-fit values used in this work.

The statistical quantity of importance when comparing two models is the reduced  $\chi^2$  value<sup>22</sup>,  $\chi_v^2$ . The  $\chi_v^2$  value is normalized by the uncertainty,  $\epsilon$ , which is determined by FEFFIT and includes only an average statistical error; therefore, values reported for  $\chi_v^2$  are poorly scaled and often as large as several hundred. Because  $\epsilon$  is the same value for all fits to the same experimental data, only a qualitative comparison of the  $\chi_v^2$  values for each model is required. A significant change from the initial  $\chi_{iv}^2$  to the final  $\chi_{fv}^2$ , determined by two standard deviations, is defined as

$$\frac{\chi_{iv}^2}{\chi_{fv}^2} - 1 \geq 2\sqrt{\frac{2}{v}} \quad (1)$$

Another goodness-of-fit parameter is the sum of the fractional error,  $R$ -factor.<sup>22</sup> An  $R$ -factor value below 5% indicates that the model is reasonable. Thus, the large  $\chi^2$  values are a result of excluding systematic errors in  $\epsilon$ .

The uncertainties in our fitted parameters have been multiplied by  $\chi_v^2$  to include the uncertainty in systematic errors.

#### IV. Cu K-Edge Data of Cu<sub>2</sub>O Standard

$N_{\text{degen}}$  and  $S_0^2$  are both constant multiplication factors in the XAFS theory used to construct the models. Therefore, only the product  $N_{\text{degen}}S_0^2$  can be determined. Cu K-edge data for a Cu<sub>2</sub>O standard were collected to decouple these constants. The crystallographic structure for Cu<sub>2</sub>O is known, so  $N_{\text{degen}}$  is no longer a fitted parameter. The value for  $S_0^2 = 0.82 \pm 0.10$  was determined.

#### V. Cu K-edge Data

The Cu K-edge data were aligned, and the background was removed according to the standard procedure described in section III.  $E_0$  and  $R_{\text{bkg}}$  input parameters were 8986 eV and 0.8 Å, respectively. Two data sets were collected for each sample at both room temperature and ~100 K. The resulting  $\chi(k)$  for each temperature were averaged.

**A. X-Ray Absorption Near-Edge Structure.** X-ray-absorption near-edge structure (XANES) can be used to determine the valence state of the absorbing atom as well as its locale environment. Figure 4 compares the normalized absorption XANES data taken on the sample to that taken on the SAMMS + AsO<sub>4</sub> and the SAMMS + CrO<sub>4</sub> samples, respectively. For each data set shown in the figure, both scans are over plotted to show that the features are reproducible. In both cases, the addition of AsO<sub>4</sub> or CrO<sub>4</sub> resulted in a slight change in the shape of the edge, denoted by the arrows in the figure. This change indicates that AsO<sub>4</sub> or CrO<sub>4</sub> is having a slight effect on the average local structure of Cu in the SAMMS samples. The edge position and overall shape of the XANES spectra are similar,

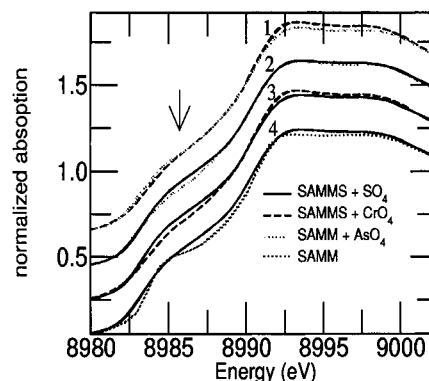


**Figure 4.** XANES Cu K-edge data. Two scans for each data set are plotted in the figure illustrating the reproducibility of the edge features. Comparison of two different data sets: (1) SAMMS samples with AsO<sub>4</sub> and CrO<sub>4</sub>, (2) SAMMS sample with and without AsO<sub>4</sub>, (3) SAMMS sample with and without CrO<sub>4</sub>, and (4) SAMMS sample with and without SO<sub>4</sub>.

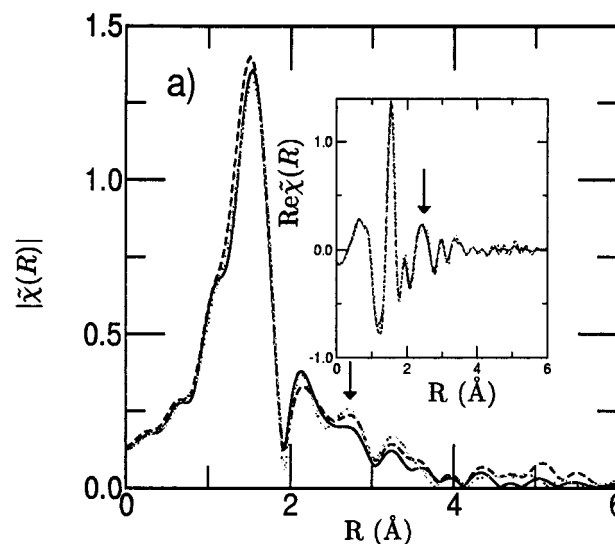


**Figure 5.** Fourier transform of the Cu K-edge data from the SAMMS + SO<sub>4</sub> (light dotted), SAMMS + SO<sub>4</sub>/CrO<sub>4</sub> (dashed), and SAMMS + SO<sub>4</sub>/AsO<sub>4</sub> (solid) samples. (a) The magnitude of the Fourier transform. (inset) The real part of the Fourier transform. The arrow shows a decrease in the amplitude of the Fourier transform that is due to SO<sub>4</sub>/CrO<sub>4</sub> anions.

indicating that the Cu anion has not changed its valence state from Cu(II).

**B. Model and Results.** Figure 5 compares the  $|\tilde{\chi}(R)|$  and  $\text{Re}\tilde{\chi}(R)$  data taken at ~100 K for the SAMMSs samples with a complex anion. The region of the data between 2.4 and 3.2 Å shows a slight decrease in amplitude that is due to the presence of AsO<sub>4</sub>/CrO<sub>4</sub> anions. The gross features of the Fourier transform of the data from all three samples are similar, indicating that most of the Cu sites have the same local structure in all three samples. The structure in this region of Figure 5 is complicated because of the contribution from many atoms at approximately the same radial distance from the Cu atom and because no dramatic change in the data indicates the presence of the As/Cr atoms. Elemental analysis indicates that 20% of the SO<sub>4</sub> is still present, with AsO<sub>4</sub> and CrO<sub>4</sub> in both of the samples. The positions of the As and Cr atom relative to the Cu atom are of primary concern. Therefore, the SAMMS + SO<sub>4</sub> data were analyzed in detail first, and then the best-fit model was applied to the other data sets. Finally, after the As and Cr

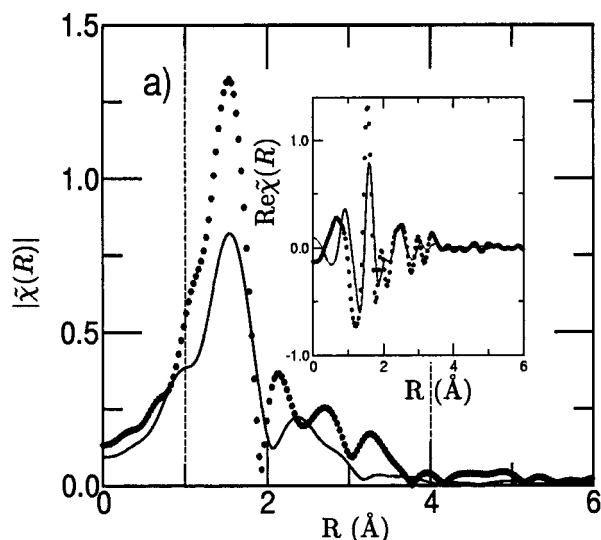


**Figure 6.** Fourier transform of the Cu K-edge data from the SAMMS + SO<sub>4</sub> and SAMMS samples. (a) The magnitude of the Fourier transform. (inset) The real part of the Fourier transform. The data illustrate the change in the local environment of the Cu atom due to complexing of the anion.

K-edge data were analyzed, a multiedge fit was performed to confirm the atomic distance from the Cu atoms to the As/Cr atoms.

In contrast to the Fourier transform of the Cu K-edge data for the samples with a bound anion, shown in Figure 5, Figure 6 compares the  $|\tilde{\chi}(R)|$  and  $\text{Re}\tilde{\chi}(R)$  data for the SAMMS + SO<sub>4</sub> and the SAMMS samples. The large differences in overall structure, peak positions, and heights of the Fourier transform between these two data sets indicates a large change in the average local environment about the Cu when the anion is or is not bound to the Cu complex. Therefore, the model and fit results for the SAMMS data are treated separately below.

**1. SAMMS.** A three-dimensional model of Cu(EDA)<sub>3</sub> (see Figure 1) of the SAMMSs was calculated previously.<sup>14</sup> The H atoms bound to each C and N atom are not shown to simplify the figure. Starting with this model, we constructed several trial structures and tested their ability to reproduce the XAFS data shown in Figure 7. We found that a model consisting of one N and three C shells was statistically better than a model consisting of one N and two C shells, which corresponds to the structure shown in Figure 1. The  $\chi^2$  was reduced from 122 to 84 with six independent points in the fit. In both cases, the degeneracy of the N and C shells was close to 6 and 3, respectively. This model was simultaneously fitted to the data with k-weighting values of 1, 2, and 3 in the Fourier transform of the data to decrease the correlation between the degeneracy and  $\sigma_i^2$  values for the theoretical model. The variables used in the best-fit model are listed in Table 2, and the best-fit values for the structural parameters are listed in Table 3.

**2. SAMMS + SO<sub>4</sub>.** When the SO<sub>4</sub> anion is introduced to the SAMMSs, several binding mechanisms are possible. Two of the lowest-energy configurations are shown in Figure 8. The computer modeling is described elsewhere.<sup>14</sup> As shown, the anion can displace an entire NH<sub>2</sub>–CH<sub>2</sub>–CH<sub>2</sub>–NH–R chain(s) and/or break off one end of a chain(s). The configuration in Figure 8a shows monodentate bonding of the SO<sub>4</sub> anion to the SAMMSs functional group, which, in this case, is composed of one closed and two open chains bonded to the Cu(II). The configuration in Figure 8b shows bidentate bonding of the SO<sub>4</sub> anion to the SAMMSs functional group, which is composed of one open and one closed chain bonded to the Cu(II). Both of

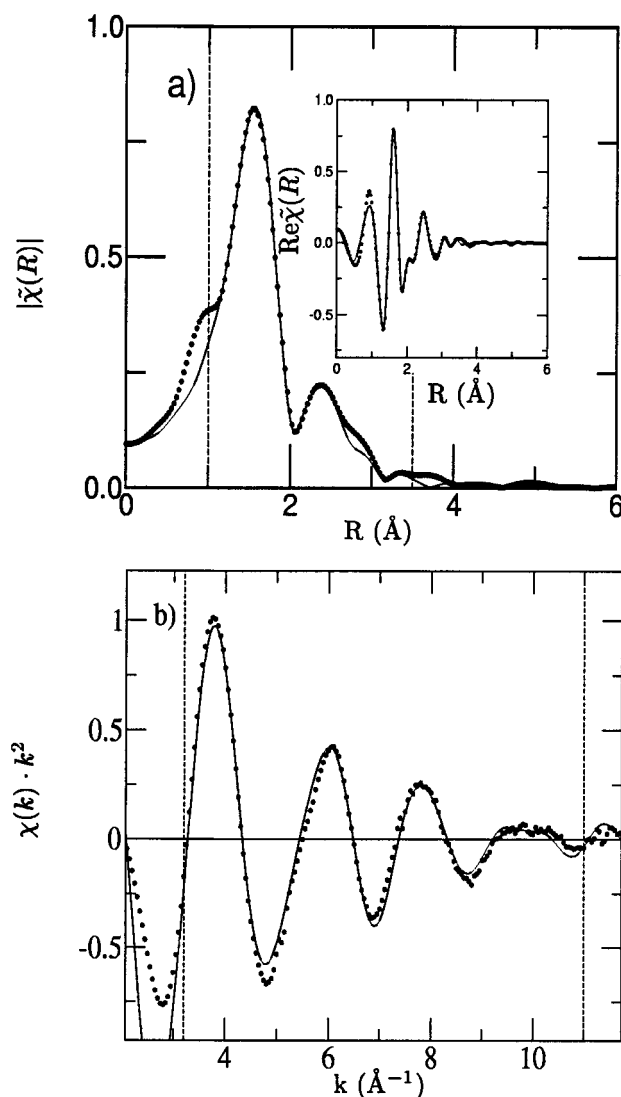


**Figure 7.** Cu K-edge data from the SAMMS sample and the model. The dashed vertical lines represent the fit range. (a) The magnitude of the Fourier transform. (inset) The real part of the Fourier transform. (b) Nonfiltered  $\chi(k)k^2$  data and model.

**TABLE 2: Parameters Used to Describe the Model for the Cu K-Edge Data for the Sample<sup>a</sup>**

atom type	$N_{\text{deg}}$	$\Delta R$	$\sigma_i^2$
Cu → N1	6	$\Delta r_1$	$\sigma_1^2$
Cu → C1	3	$\Delta r_2$	$\sigma_2^2$
Cu → C2	3	$\Delta r_3$	$\sigma_2^2$
Cu → C3	3	$\Delta r_4$	$\sigma_2^2$

<sup>a</sup> One overall energy shift and  $S_0^2$  were also determined in the fit. Total number of parameters is 8:  $\Delta E_0$ ,  $\Delta r_1$  through  $\Delta r_4$ ,  $\sigma_1^2$ ,  $\sigma_2^2$ , and  $S_0^2$ .

these structures and several others with mono-, bi-, or tridentate bonding of the SO<sub>4</sub> anion to the Cu(II) were used as input structures to FEFF7 to generate the theoretical models of the XAFS spectra for the local chemical environments about Cu in these samples.

Because each model includes many single and multiple scattering paths, several constraints were used to reduce the total number of fitted parameters. These constraints include one energy shift for the first O/N paths and another for all other paths: one  $\sigma_i^2$  value for the H paths, one  $\sigma_i^2$  for the S path, one Debye temperature for all other paths that include C, N, and O atoms (see section III), and five to nine independent  $\Delta R_i$  values,

**TABLE 3: Best-Fit Results for the Cu K-Edge Data Taken on the SAMMS Sample<sup>a</sup>**

atom type	$N_{\text{degen}}$	$R$ (Å)	$\sigma_i^2$ (Å <sup>2</sup> )
Cu $\rightarrow$ N	6	$2.07 \pm 0.01$	$0.011 \pm 0.001$
Cu $\rightarrow$ C1	3	$2.95 \pm 0.02$	$0.007 \pm 0.002$
Cu $\rightarrow$ C2	3	$3.18 \pm 0.03$	$0.007 \pm 0.002$
Cu $\rightarrow$ C3	3	$3.43 \pm 0.03$	$0.007 \pm 0.002$

<sup>a</sup>  $\Delta E_{0i} = -0.3 \pm 0.8$  eV for all paths.  $S_0^2 = 1.06 \pm 0.07$ . The fit parameters are listed in Table 2.

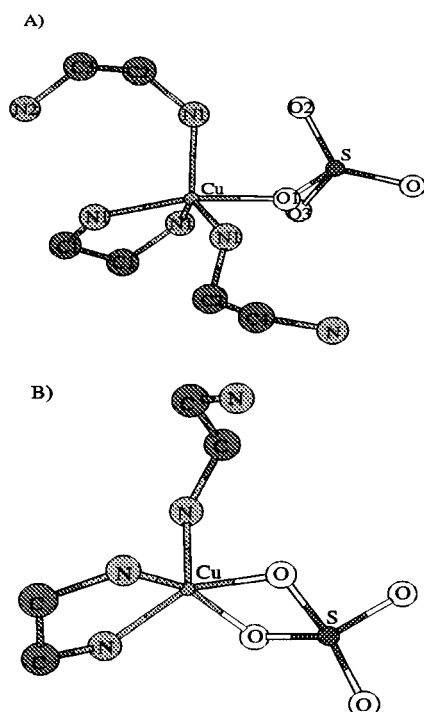


**Figure 8.** Two possible models for the structure about Cu in SAMMS + SO<sub>4</sub>. (a) Monodentate bonding of the SO<sub>4</sub> anion with one closed chain and two open chains bound to the Cu. (b) Bidentate bonding of the SO<sub>4</sub> anion with one closed and one open chain bound to the Cu. Each C and N atom has two closely bound H that are not shown for simplicity.

where several paths with the same scattering atom at approximately the same distance were constrained to have the same  $\Delta R_i$  value.  $S_0^2$  was set to  $0.82 \pm 0.10$ , as determined from a Cu standard (section IV). With these constraints, a total of 10–17 parameters were determined in the fit to the data containing 18 independent points (section III). Each of the 15 models were simultaneously fitted to three different versions of the Cu K-edge data taken on the SAMMS + SO<sub>4</sub> sample at  $\sim 100$  K processed by using a  $k$ -weighting of 1, 2, and 3 in the Fourier transform.

Table 4 lists the different SAMMSs models and their goodness-of-fit parameters (see section III) from a fit to the data taken on the SAMMS + SO<sub>4</sub> sample at  $\sim 100$  K. The model for monodentate binding of the SO<sub>4</sub> anion, along with one closed and two open chains bonded to the Cu(II) (see Figure 8a), gives a  $\chi_v^2$  value 3.4 times smaller than that for the next best model. A significant change in  $\chi_v^2$  value is 1.6 (see eq 1). Therefore, this model is statistically better than any of the other models. In addition, the XAFS results are consistent with results of previous molecular modeling studies.<sup>14</sup>

Next, the best-fit model is refined and fitted simultaneously to three different versions of the room temperature and  $\sim 100$  K data processed by using a  $k$ -weight values of 1, 2, and 3 in the Fourier transform. The final model consists of all paths with

**TABLE 4: Possible Models for the SAMMS + SO<sub>4</sub> Sample<sup>a</sup>**

model	no. of closed		goodness-of-fit values		
	SO <sub>4</sub> to Cu bonding	EDA chains	EDA chains	$R$ -factor	$\chi_v^2$ $\nu$
monodentate	2	0	0.022	614	7
monodentate	2	1	0.024	800	5
monodentate <sup>b</sup>	1	2	0.003	127	3
monodentate	1	3	0.010	594	3
monodentate	0	4	0.016	435	6
monodentate	0	5	0.015	488	6
bidentate	2	0	0.002	712	3
bidentate <sup>c</sup>	1	1	0.002	6242	1
bidentate	1	2	0.002	5614	1
bidentate	0	3	0.008	769	4
bidentate	0	4	0.022	1176	4
tridentate	1	1	0.004	1164	6
tridentate	0	3	0.056	13021	2
tridentate	0	2	0.007	737	5
tridentate	1	0	0.002	606	5

<sup>a</sup> Each model has either five or six O/N atoms about the Cu site. On the basis of energy minimization by molecular modeling codes, Figure 10 shows the two most likely configurations, denoted with the superscripts *b* and *c*.

**TABLE 5: Parameters Used to Describe the for the Cu K-Edge Data for the SAMMS + SO<sub>4</sub> Sample<sup>a</sup>**

atom type	$N_{\text{degen}}$	$\Delta R$	$\sigma_i^2$
Cu $\rightarrow$ O1	1 <sub>s</sub>	$\Delta r_1$	$T_{\text{debye}}^1$
Cu $\rightarrow$ N1	4 <sub>s</sub>	$\Delta r_1$	$T_{\text{debye}}^1$
Cu $\rightarrow$ C1	2 <sub>s</sub>	$\Delta r_2$	$T_{\text{debye}}^1$
Cu $\rightarrow$ C2	2 <sub>s</sub>	$\Delta r_2$	$T_{\text{debye}}^1$
Cu $\rightarrow$ C1 $\rightarrow$ N1	4 <sub>s</sub>	$\Delta r_3$	$T_{\text{debye}}^1$
Cu $\rightarrow$ S	1 <sub>s</sub>	$\Delta r_4$	$T_{\text{debye}}^1$
Cu $\rightarrow$ O2	1 <sub>s</sub>	$\Delta r_5$	$T_{\text{debye}}^1$
Cu $\rightarrow$ O3	1 <sub>s</sub>	$\Delta r_5$	$T_{\text{debye}}^1$
Cu $\rightarrow$ N1 $\rightarrow$ N1	2 <sub>s</sub>	$\Delta r_6$	$T_{\text{debye}}^1$
Cu $\rightarrow$ C3	1 <sub>s</sub>	$\Delta r_7$	$T_{\text{debye}}^1$
Cu $\rightarrow$ O1 $\rightarrow$ N1	2 <sub>s</sub>	$\Delta r_8$	$T_{\text{debye}}^1$
Cu $\rightarrow$ O1 $\rightarrow$ Cu $\rightarrow$ N1	2 <sub>s</sub>	$\Delta r_8$	$T_{\text{debye}}^1$
Cu $\rightarrow$ N2	1 <sub>s</sub>	$\Delta r_9$	$T_{\text{debye}}^1$
Cu $\rightarrow$ C4 $\rightarrow$ N1	2 <sub>s</sub>	$\Delta r_{10}$	$T_{\text{debye}}^1$

<sup>a</sup> One energy shift for all paths was also determined in the fit. Total number of parameters is 12:  $\Delta E_{0i}$ ,  $\Delta r_1$  through  $\Delta r_{10}$ , and  $T_{\text{debye}}$ .<sup>1</sup>

a plane-wave amplitude ratio greater than 15% of the first Cu  $\rightarrow$  O path, for a total of 14 paths described with 12 parameters. These parameters are listed in Table 5. The use of a Debye temperature to parametrize the values for  $\sigma_i^2$  is discussed in section III. The data and fit ranges listed in Table 1 result in 18.2 independent points.

The results from the fit of this model to the data are listed in Table 6. The best-fit values for  $\sigma_i^2$  are all positive and less than 0.010 Å<sup>2</sup>,  $\Delta E_{0i}$  is consistently less than 2 eV, and  $\Delta R_i$  values are not more than 0.37 Å from those in the starting model. The  $|\tilde{\chi}(R)|$  and  $Re\tilde{\chi}(R)$  data and model are shown in Figure 3. This figure illustrates the goodness-of-fit of the model to the experimental data. The data and fit ranges, along with the Fourier transform parameters, are in Table 1.

3. *SAMMS + SO<sub>4</sub>/AsO<sub>4</sub> and SAMMS + SO<sub>4</sub>/CrO<sub>4</sub>.* The model described in the previous section was applied to the Cu K-edge data of the SAMMS + SO<sub>4</sub>/AsO<sub>4</sub> and SAMMS + SO<sub>4</sub>/CrO<sub>4</sub> samples. The amplitude of the S path was reduced to 20%, and an As/Cr path with an amplitude of 80% was added to the model to account for an 80% displacement of S by As/Cr, as determined by elemental analysis. The results are similar to those reported in the previous subsection for SAMMS + SO<sub>4</sub> the sample. Table 6 lists the best-fit values for each of these data sets.

**TABLE 6: Best-Fit Results for the Cu K-Edge Data Taken on the SAMMS + SO<sub>4</sub>, SAMMS + SO<sub>4</sub>/AsO<sub>4</sub>, and Samples<sup>a</sup>**

atom type	$N_{\text{deg}}$	SAMMS + SO <sub>4</sub>		SAMMS + SO <sub>4</sub> /AsO <sub>4</sub>		SAMMS + SO <sub>4</sub> /CrO <sub>4</sub>	
		$R$ (Å)	$\sigma_i^2$ ( $\times 10^3$ Å <sup>2</sup> )	$R$ (Å)	$\sigma_i^2$ ( $\times 10^3$ Å <sup>2</sup> )	$R$ (Å)	$\sigma_i^2$ ( $\times 10^3$ Å <sup>2</sup> )
Cu → O1	1	1.98 ± 0.01	4 ± 1	1.98 ± 0.01	4 ± 1	1.97 ± 0.01	4 ± 1
Cu → N1	4	2.02 ± 0.01	4 ± 1	2.02 ± 0.01	5 ± 1	2.01 ± 0.01	4 ± 1
Cu → C1	2	2.89 ± 0.07	6 ± 1	2.91 ± 0.07	6 ± 1	2.90 ± 0.05	5 ± 1
Cu → C2	2	3.14 ± 0.07	6 ± 1	3.16 ± 0.07	6 ± 1	3.15 ± 0.05	5 ± 1
Cu → S	1	3.20 ± 0.07	3 ± 1				
Cu → S	0.2			2.98 ± 0.17	3 ± 1	3.14 ± 0.18	2 ± 1
Cu → As	0.8			3.31 ± 0.03	2 ± 1		
Cu → Cr	0.8					3.39 ± 0.03	2 ± 1
Cu → O2	1	3.28 ± 0.12	4 ± 1	3.40 ± 0.45	4 ± 1	3.38 ± 0.50	4 ± 1
Cu → O3	1	3.36 ± 0.12	4 ± 1	3.48 ± 0.45	4 ± 1	3.46 ± 0.50	4 ± 1
Cu → C3	1	3.41 ± 0.35	6 ± 1	3.50 ± 1.80	6 ± 1	3.48 ± 1.40	7 ± 1
Cu → N2	1	4.23 ± 0.24	5 ± 1	4.24 ± 0.50	5 ± 1	4.22 ± 0.30	5 ± 1

<sup>a</sup>  $\Delta E_{0i}$  = 1.1, 1.4, and  $0.8 \pm 1$  eV for all paths, for each data set, respectively.  $S_0^2$  was set at  $0.82 \pm 0.10$ , as determined from a Cu standard (see section IV). The fit parameters are in Table V.

## VI. As and Cr K-Edge Data

The SAMMS + SO<sub>4</sub>/AsO<sub>4</sub> and SAMMS + SO<sub>4</sub>/CrO<sub>4</sub> data were aligned, and the backgrounds were removed according to the standard procedure described in section III.

For the As XAFS data taken on the SAMMS + SO<sub>4</sub>/AsO<sub>4</sub> sample, the input parameters to AUTOBK are  $E_0$  (set to the value at half the normalized edge step) and  $R_{\text{bkg}} = 1.0$  Å. Data were collected at room temperature and  $\sim 100$  K. At each temperature, the resulting  $\chi(k)$  values were averaged. The average measurement uncertainty in  $k$ -space of the averaged data is 0.3%.

For the Cr XAFS data taken on the SAMMS + SO<sub>4</sub>/CrO<sub>4</sub> sample, the input parameters to AUTOBK are  $E_0$  (set to the value at half the normalized edge step) and  $R_{\text{bkg}} = 1$  Å. Three data sets were collected at room temperature, and the resulting  $\chi(k)$  values were averaged. The average measurement uncertainty of the averaged data set in  $k$ -space is 0.3%.

**A. Near-Edge Features.** The average local symmetry about As and Cr can be determined from the edge features of the normalized absorption data. Figure 9a shows the Cr K-edge of the normalized absorption data from the SAMMS + SO<sub>4</sub>/CrO<sub>4</sub> sample. The large preedge feature, denoted by the arrow in the figure, signifies the tetrahedral structure of Cr(VI).<sup>25</sup> Figure 9b shows the As K-edge of the normalized absorption data from the SAMMS + SO<sub>4</sub>/AsO<sub>4</sub> sample and a As<sub>2</sub>O<sub>3</sub> standard for comparison. An average energy difference of  $4 \pm 1$  eV between these edges indicates that the average valence state of the As bound to the SAMMSs is 5. As(V) typically exists in a tetrahedral structure. Although the figure shows only the  $\sim 100$  K measurements, this shift was also found for the room-temperature measurements.

**B. Model and Results.** The model for the As/Cr K-edge data is based on the structure shown in Figure 8a. The model for the As K-edge data (see Table 7) includes an oxygen path, a triangle oxygen path, a copper path, and a nearly linear oxygen–nitrogen path. The parameters determined in the fit are  $\Delta E_{01}$  for the first oxygen path,  $\Delta E_{02}$  for the triangle oxygen path and copper path, a weighted average of  $\Delta E_{01}$  and  $\Delta E_{02}$  for the oxygen–nitrogen path, a  $T_{\text{debye}}$  and  $\Delta R_i$  value for each path, and an  $S_0^2$  value. The model is fit simultaneously to three different versions of the room temperature and  $\sim 100$  K data processed by using a  $k$ -weighting of 1, 2, and 3 in the Fourier Transform. The room-temperature data is allowed one more parameter,  $\alpha$ , the compression relative to the low-temperature data. The temperature dependence of the triangle oxygen path was not well described by the correlated Debye Model with a single  $T_{\text{debye}}$ . This is most likely due to static disorder in the

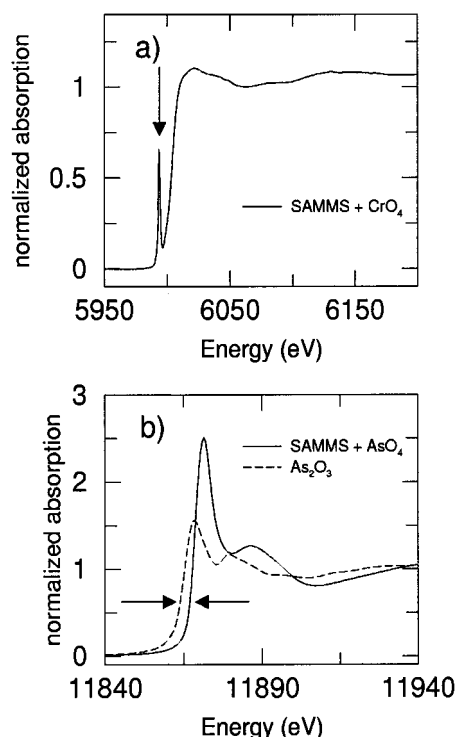


**Figure 9.** XANES of the (a) Cr K-edge data from the SAMMS + CrO<sub>4</sub> sample and (b) As K-edge data from the SAMMS + SO<sub>4</sub>/AsO<sub>4</sub> sample and an As<sub>2</sub>O<sub>3</sub> standard.

**TABLE 7: Best-Fit Results for the As K-Edge Data Taken on the SAMMS + SO<sub>4</sub>/AsO<sub>4</sub> Sample<sup>a</sup>**

atom type	$N_{\text{deg}}$	$R$ (Å)	$\sigma_i^2$ (Å <sup>2</sup> )	$\Delta E_{0i}$ (eV)
As → O1	4	1.70 ± 0.01	0.002 ± 0.001	11 ± 1
As → O1 → O1	12	3.06 ± 0.07	0.014 ± 0.002	6 ± 3
As → Cu	1	3.22 ± 0.10	0.010 ± 0.011	6 ± 3
As → O1 → N1	2	4.17 ± 0.08	0.004 ± 0.007	8 ± 2

<sup>a</sup>  $S_0^2 = 0.99 \pm 0.06$ . The best-fit value for  $\epsilon = 0.0 \pm 0.6\%$  is consistent with no compression of the  $\sim 100$  K data compared to the room-temperature data.

path length. Therefore, individual  $\sigma_i^2$  values were used for room temperature and  $\sim 100$  K, giving this model a total of 11 variables plus 3 additional variables that depend only on the room-temperature data. Both the room temperature and  $\sim 100$  K data contain 20 independent points (see section III).

The model for the room temperature Cr K-edge data (see Table 8) includes two oxygen paths, two nitrogen paths, a copper path, and a nearly linear oxygen–nitrogen path.<sup>29</sup> The param-



**TABLE 8: Best-Fit Results for the Cr K-Edge Data Taken on the Sample<sup>a</sup>**

atom type	$N_{\text{deg}}$	$R$ (Å)	$\sigma_i^2$ (Å <sup>2</sup> )
Cr → O1	2	$1.65 \pm 0.01$	$0.002 \pm 0.001$
Cr → O1	2	$1.99 \pm 0.01$	$0.002 \pm 0.001$
Cr → N1	1	$3.03 \pm 0.03$	$0.011 \pm 0.003$
Cr → N1	1	$3.10 \pm 0.03$	$0.011 \pm 0.003$
Cr → Cu	1	$3.29 \pm 0.02$	$0.011 \pm 0.002$
Cr → O1 → N1	2	$4.10 \pm 0.03$	$0.005 \pm 0.003$

<sup>a</sup>  $\Delta E_{0i} = -7 \pm 1$  eV for all paths.  $S_0^2 = 1.07 \pm 0.11$ .

eters determined in the fit are (1) a  $\Delta R_i$  and  $\sigma_i^2$  value for each path, except that the  $\sigma_i^2$  values for the Cr → O paths are constrained to be equal and the two Cr → N paths have the same  $\sigma_i^2$  and  $\Delta R_i$  values, (2) an overall  $\Delta E_{0i}$ , and (3) a single  $S_0^2$  value. This model has a total of 11 variables, and the data contain 16 independent points (see section III). As required, both models have fewer parameters than independent points in the data.

The best-fit results for the As/Cr K-edge data are listed in Tables 7 and 8, respectively. The values for  $\sigma_i^2$  are not more than 0.012 Å<sup>2</sup>, and the value for the distance to each of the shells is within 0.40 Å of the distance in the starting model. The Fourier transform of the As/Cr K-edge data and the models are shown in Figures 10 and 11, respectively. The Fourier transform parameters are in Table 1. The magnitude of the first-shell peak of the Cr K-edge data is less than half that of the As K-edge data. This decrease is due to a large splitting, 0.34 Å, of the oxygen tetrahedra for CrO<sub>4</sub>, whereas the oxygen tetrahedra for AsO<sub>4</sub> are not split (see Tables 7 and 8). A split oxygen shell can be included in the model for the As K-edge data but was found to be unnecessary by comparison of the  $\chi^2$  values and by the fit results for the split oxygen distances which were found to be equivalent. This difference in tetrahedral structure compares well with some other known AsO<sub>4</sub> and CrO<sub>4</sub> structures. For example, FeAsO<sub>4</sub>·2(H<sub>2</sub>O) has four As → O bond lengths of 1.67–1.69 Å, whereas K<sub>2</sub>Cr<sub>2</sub>O<sub>7</sub> has two short Cr → O bond lengths of 1.52 and 1.54 Å and two long Cr → O bond lengths of 1.73 and 1.85 Å.<sup>26</sup> Another result is a single Cr → Cu and As → Cu distance of approximately 3.2 Å (see Tables 7 and 8). This compares well with the Cu → S distance from the Cu K-edge data on the SAMMS + SO<sub>4</sub> sample listed in Table 6 and is further evidence of the monodentate bonding between the AsO<sub>4</sub>/CrO<sub>4</sub> anion and the Cu EDA in the SAMMSs. Other evidence of monodentate binding of the anion to the SAMMSs is the nearly linear As/Cr → O → N path at approximately 4.1 Å. This signal is particularly interesting because it gives evidence for the binding mechanism and stereochemistry between the anion and the Cu-EDA end member of the SAMMSs and was predicted in the model for monodentate binding, shown in Figure 8a.

## VII. Simultaneous Cu, As, and Cr K-Edge Data Fit

Although the individual fit results from each SAMMSs measurement agree reasonably well with each other for the As, Cr, and S distances from the Cu(II) anion, we can refine these results by performing a simultaneous fit to all the data. Each data set contains some signal in common with at least one other data set. Therefore, there are common fit parameters for all the data sets. We determined these simultaneously. For example, the XAFS signal from the Cu → As path in the Cu K-edge data containing AsO<sub>4</sub> has many of the same XAFS parameters as the XAFS signal from the As → Cu path in the As K-edge data. Both of these data sets can be fitted simultaneously by using the same XAFS parameters for these common paths. This

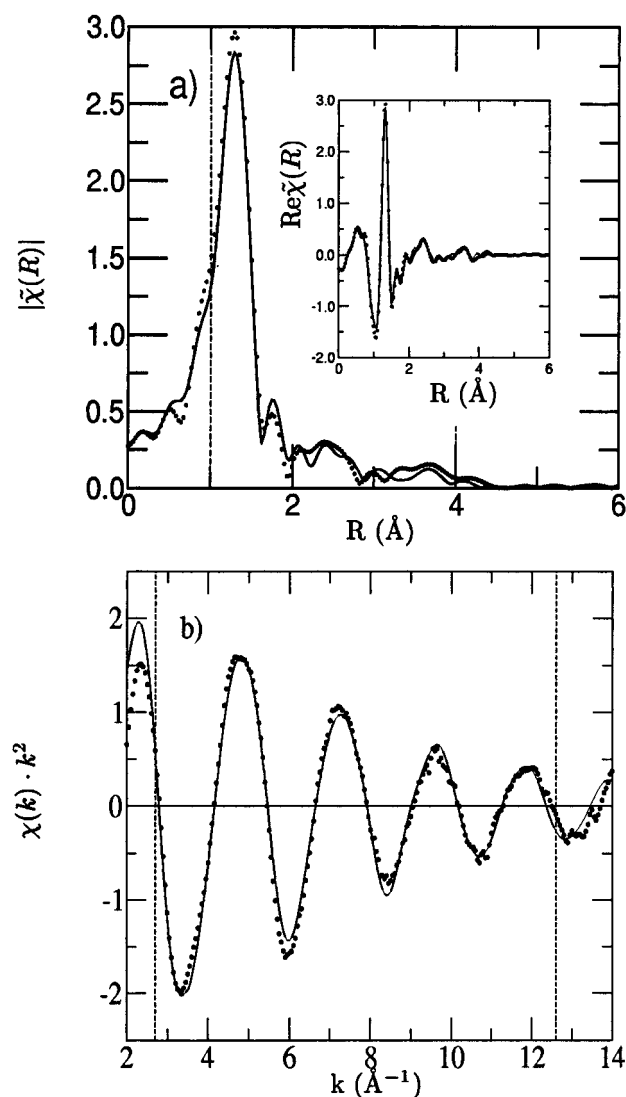


**Figure 10.** Fourier transform of the As K-edge data from the SAMMS + SO<sub>4</sub>/AsO<sub>4</sub> sample at ~100 K and the model. The dashed vertical lines represent the fit range. (a) The magnitude of the Fourier transform. (inset) The real part of the Fourier transform. (b) Nonfiltered  $\chi(k)k^2$  data and model.

process ensures consistent results for the distance between atoms and relative mean square displacements. Table 9 lists the paths that are present in more than one data set. All other paths that are not listed in Table 9 were determined independent of the values for each data set. For example, the parameters for the Cu → O2 path of the SAMMS + SO<sub>4</sub>/AsO<sub>4</sub> data were not constrained by the parameters for the Cu → O2 path of the SAMMS + SO<sub>4</sub>/CrO<sub>4</sub> data. We fitted a total of seven data sets by using the models described in the previous sections. The data sets include the Cu K-edge data containing AsO<sub>4</sub> and CrO<sub>4</sub>, the As K-edge data from the SAMMS + SO<sub>4</sub>/AsO<sub>4</sub> sample, the Cr K-edge data from the SAMMS + SO<sub>4</sub>/CrO<sub>4</sub> sample, and the Cu K-edge data from the SAMMS + SO<sub>4</sub> sample. The refined values for the paths constrained by more than one data set (Table 10) are consistent with the values determined from each edge independently (Tables VI, VII, and VIII). We have simply reduced the uncertainties in our reported values.

## VIII. Conclusions

The XAFS analysis of the Cu K-edge data from the unladen SAMMS sample indicates that the Cu(EDA)<sub>3</sub> complex is



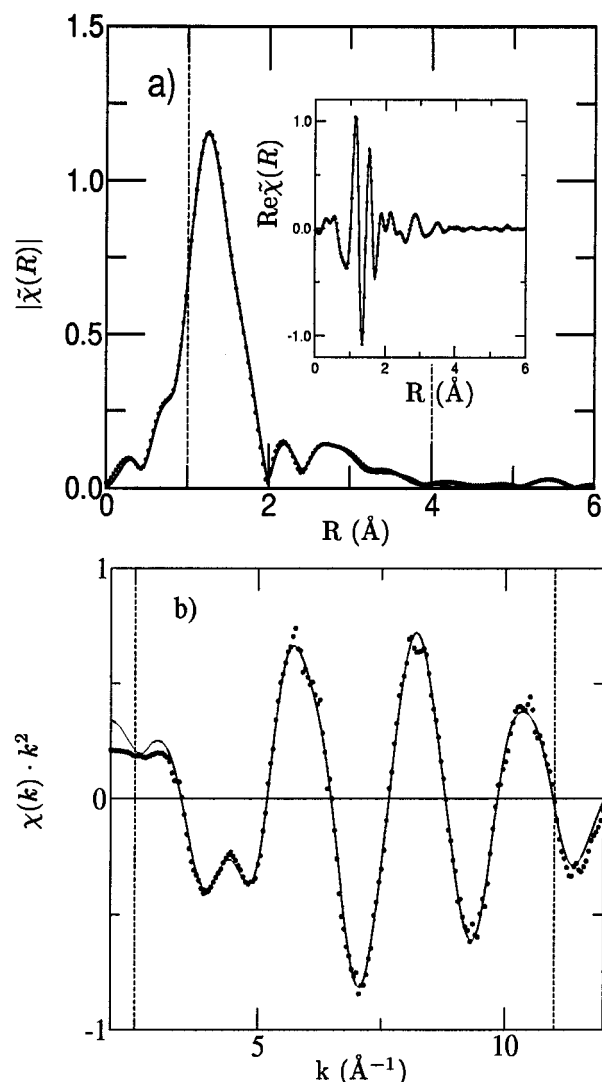


**Figure 11.** Fourier transform of the Cr K-edge data from the SAMMS + SO<sub>4</sub>/CrO<sub>4</sub> sample at room temperature and the model. The dashed vertical lines represent the fit range. (a) The magnitude of the Fourier transform. (inset) The real part of the Fourier transform. (b) Nonfiltered  $\chi(k)k^2$  data and model.

**TABLE 9: Paths that Are Common to More than One Data Set**

data description	Cu ↔ S	Cu ↔ As	Cu ↔ Cr
Cu K-edge, SAMMS + SO <sub>4</sub> /AsO <sub>4</sub>	×	×	
Cu K-edge, SAMMS + SO <sub>4</sub> /CrO <sub>4</sub>	×		×
Cu K-edge, SAMMS + SO <sub>4</sub>	×		
Cr K-edge, SAMMS + SO <sub>4</sub> /CrO <sub>4</sub>			×
As K-edge, SAMMS + SO <sub>4</sub> /AsO <sub>4</sub>		×	

**TABLE 10: Best-Fit Results for Cu K-Edge SAMMS + SO<sub>4</sub>/AsO<sub>4</sub>, SAMMS + SO<sub>4</sub> and SAMMS + SO<sub>4</sub>/CrO<sub>4</sub> Data As K-Edge SAMMS + SO<sub>4</sub>/AsO<sub>4</sub> Data and Cr K-Edge SAMMS + SO<sub>4</sub>/CrO<sub>4</sub> Data<sup>a</sup>**

atom type	$N_{\text{deg}}$	$R$ (Å)	$\sigma_i^2$ (Å <sup>2</sup> )
Cu → S	0.20	$3.19 \pm 0.06$	$0.002 \pm 0.013$
Cu → As	0.80	$3.28 \pm 0.05$	$0.013 \pm 0.008$
Cu → Cr	0.80	$3.31 \pm 0.06$	$0.012 \pm 0.007$

<sup>a</sup> A simultaneous fit was performed, and the values shown above were refined.

octahedral (see Figure 1) which forms the stereospecific cationic template for those anions with C<sub>3</sub> symmetry. The relatively large change in the signal of the Fourier transform of the data in the

unladen SAMMS sample versus the laden SAMMS sample shows that the average local Cu environments changes dramatically when an anion is bound to the Cu(EDA)<sub>3</sub> complex (see Figure 6).

The XAFS analysis of the Cu K-edge data from the SAMMS + SO<sub>4</sub> sample indicates that the structure is best described with monodentate binding of the SO<sub>4</sub> anion to the Cu(II) ion, with one chelating EDA ligand and two open NH<sub>2</sub>–CH<sub>2</sub>–CH<sub>2</sub>–NH–R chains also bound to the Cu(II) ion through the secondary amine, resulting in a trigonal bipyramidal geometry (see Figure 10a). The confidence in the model is based on three factors: (1) Statistically, the fit to the data is better than for any of the other models listed in Table 4. (2) The fit parameters are reasonable for the model. (3) This model is one of the lowest-energy configurations from molecular modeling studies. This structure is consistent with the lock-and-key mechanism described previously,<sup>14</sup> where the anion binding affinity involves a stepwise association of the tetrahedral oxoanion to the Cu(EDA)<sub>3</sub> complex, followed by displacement of the amine terminus from two EDA ligands by the oxoanion.

The consistent change in the shape of the normalized-absorption Cu K-edge data from the SAMMS + SO<sub>4</sub> sample to the SAMMS + SO<sub>4</sub>/AsO<sub>4</sub> and SAMMS + SO<sub>4</sub>/CrO<sub>4</sub> samples indicates that AsO<sub>4</sub>/CrO<sub>4</sub> is affecting the average local Cu environment (see Figure 4). The similarity between the Cu K-edge XAFS data taken on all three loaded samples is consistent with the replacement of the SO<sub>4</sub> anion by the AsO<sub>4</sub>/CrO<sub>4</sub> anion, with the same average local environment about the Cu(II) (see Figure 5). A comparison of the Fourier transform of the Cu K-edge data from each sample shows a gradual decrease in the amplitude in the region between 2.4 and 3.2 Å (see Figure 5). The XAFS analysis of the data in this region indicates that the decrease can be accounted for by displacement of 80% of the SO<sub>4</sub> by AsO<sub>4</sub>/CrO<sub>4</sub> for the data from both the SAMMS + SO<sub>4</sub>/AsO<sub>4</sub> and SAMMS + SO<sub>4</sub>/CrO<sub>4</sub> samples. The distance between the Cu(II) ion and the oxoanion varies from 3.19 to  $3.31 \pm 0.06$  Å (see Table 10), but the geometry and stereochemistry of the EDA/anion ligand field bound to the Cu(II) ion is the same for each of the oxoanions studied. This result is consistent with the selectivity of the Cu(EDA)<sub>3</sub> anion being dictated by the ability of the anion to dissociate from the adduct. Anions that are reversibly bound (SO<sub>4</sub>) can be displaced by those that do not dissociate once bound (AsO<sub>4</sub>/CrO<sub>4</sub>).

The As/Cr K-edge features for the data taken on the SAMMS sample indicate that the average local symmetry about the As/Cr is tetrahedral and that no inorganic precipitate has formed (because there is no signal in the Fourier transform of the As/Cr K-edge data indicating a near-neighbor As/Cr atom). The large decrease in amplitude of the first peak in the Fourier transform of the XAFS data (see Figure 10 and Figure 11) in the Cr K-edge data compared to the As K-edge data is due to a large splitting of the Cr–O distances in the tetrahedral about Cr. The As and Cr K-edge data indicate that the AsO<sub>4</sub> tetrahedra consists of four As–O distances of  $1.71 \pm 0.01$  Å, whereas the CrO<sub>4</sub> tetrahedra consist of two short and two long Cr–O distances at  $1.65 \pm 0.01$  Å and  $1.99 \pm 0.01$  Å from the Cr. These differences in tetrahedral environments compare well with those of some other known AsO<sub>4</sub> and CrO<sub>4</sub> tetrahedral species. We also determined a signal in the Fourier transform of the data due to multiple scattering paths connecting the tetrahedral anion to the Cu– complex, as predicted in the model shown in Figure 8a. This result gives strong evidence for monodentate binding and the particular binding geometry shown in Figure 8a, which is consistent with the average local Cu structure as

determined from the Cu K-edge. A simultaneous fit of all Cu, As, and Cr K-edge data from the loaded SAMMSs gives consistent and refined values for the structure about the Cu(II) ions and the As, Cr, and S atoms of the complexed oxoanions.

The results presented herein support the conclusion that tetrahedral oxometalate anions are bound directly to the metal center of Cu-EDA SAMMS through a direct Cu–O bond in a monodentate fashion. Previous competition studies have shown that sulfate, once sorbed, is displaceable from the interfacial complex, but chromate and arsenate are not. These XAFS studies have revealed that this difference in chemistry is not due to different binding geometries but, rather, to an inherent difference in the dissociability of the respective anions (which parallels the solubilities of the respective copper salts).

During the process of oxoanion binding, the copper center undergoes a geometry change from octahedral to trigonal bipyramidal. This is accomplished by the loss of the two weakly held apical ligands and the association of the oxoanion to the coordinatively unsaturated Cu center. The net result is the loss of two primary amines from two separate EDA ligands and a direct Cu–O bond. This leaves the Cu coordination sphere filled with one chelating EDA ligand, two coordinated secondary amines, and the bound oxoanion. The loss of symmetry that accompanies this geometrical change alleviates any orbital degeneracy, thereby enhancing the stability of the interfacial complex. This enhanced stability, coupled with the lack of dissociation observed with the oxometalate anions, suggests that these laden SAMMS may very well have excellent long-term stability as waste forms.

**Acknowledgment.** This work was supported by the U.S. Department of Energy, Assistant Secretary for Environmental Management, Environmental Management Science Program, under Contract W-31-109-Eng-38. Use of the Advanced Photon Source was supported by the U.S. Department of Energy, Office of Science, Office of Basic Energy Sciences, under Contract W-31-109-ENG-38. MRCAT is supported by the Department of Energy under Contracts DE-FG01-94-ER45525 and the member institutions. Research carried out (in part) at the National Synchrotron Light Source, Brookhaven National Laboratory, was also supported by the Office of Basic Energy Sciences.

## References and Notes

- (1) Nickson, R.; McAuthur, J.; Burgess, W.; Ahmed, K. M.; Ravenscroft, P.; Rahman, M. *Nature* **1998**, *395*, 338.
- (2) Ahmann, D.; Krumholz, L. R.; Hemond, H. F.; Lovley, D. R.; Morel, F. M. M. *Environ. Sci. Technol.* **1997**, *31*, 2923–2930. Peters, S. C.; Blum, J. D.; Klaue, B.; Karagas, M. R. *Environ. Sci. Technol.* **1999**, *33*, 1328–1333.
- (3) Wilkie, J. A.; Hering, J. G. *Environ. Sci. Technol.* **1998**, *33*, 657–662.
- (4) Davis, A.; De Curnou, P.; Eary, L. E. *Environ. Sci. Technol.* **1997**, *31*, 1975–1991.
- (5) Feng, X.; Fryxell, G. E.; Wang, L. Q.; Kim, A. Y.; Liu, J.; Kemner, K. *Science* **1997**, *276*, 923–926.
- (6) Liu, J.; Feng, X.; Fryxell, G. E.; Wang, L. Q.; Kim, A. Y.; Gong, M. *Adv. Mater.* **1998**, *10*, 161–165.
- (7) Feng, X.; Rao, L.; Mohs, T. R.; Xu, J.; Xia, Y.; Fryxell, G. E.; Liu, J.; Raymond, K. N. In *Ceramic Transactions, Volume 93, Environmental Issues and Waste Management Technologies in the Ceramic and Nuclear Industries (IV)*; Marra, J. C., Chandler, G. T., Eds.; 1999; pp 35–42.
- (8) Mattigod, S.; Fryxell, G. E.; Feng, X.; Liu, J. In *Metal Separation Technologies Beyond 2000: Integrating Novel Chemistry with Processing*; Papiere, E., Dekker, M., Eds.; The Minerals, Metals and Materials Society: 1999; pp 71–79.
- (9) Liu, J.; Fryxell, G. E.; Qian, M.; Wang, L. Q.; Wang, Y. *Appl. Chem.* **2000**, *72*, 269–379.
- (10) Liu, J.; Fryxell, G. E.; Mattigod, S. V.; Zemanian, T. S.; Shin, Y.; Wang, L. Q. *Studies in Surface Science and Catalysis*; Elsevier: New York, 2000; Vol. 129, pp 729–738.
- (11) Mattigod, S. V.; Feng, X.; Fryxell, G. E.; Liu, J.; Gong, M. *Sep. Sci. Technol.* **1999**, *34*, 2329–2345.
- (12) Kemner, K. M.; Feng, X.; Liu, J.; Fryxell, G. E.; Wang, L. Q.; Kim, A. Y.; Gong, M.; Mattigod, S. V. *J. Synchrotron Radiat.* **1999**, *6*, 633–635.
- (13) Fryxell, G. E.; Liu, J.; Mattigod, S. V. *Mater. Technol. Adv.* **1999**, *14*, 188–191.
- (14) Fryxell, G. E.; Liu, J.; Houser, T. A.; Nie, Z.; Ferris, K. F.; Mattigod, S.; Gong, M.; Hallen, R. T. Design and Synthesis of Selective Mesoporous Anion Traps. *Chem. Mater.* **1999**, *11*, 2148–2154.
- (15) Stern, E. A. Structural Determination by X-ray Absorption. *Comput. Phys. Commun.* **1978**, *19* (4), 289–310.
- (16) Stern, E. A.; Heald, S. M. *Basic Principles and Applications of EXAFS. Handbook of Synchrotron Radiation*; North-Holland: New York, 1983; pp 995–1014.
- (17) Zabinsky, S. I.; Rehr, J. J.; Ankudinov, A.; Albers, R. C.; Eller, M. J. Multiple-Scattering Calculations of X-Ray-Absorption Spectra. *Phys. Rev. B* **1995**, *52* (4), 2995–3009.
- (18) Segre, C. U.; Leyarowska, N. E.; Chapman, L. D.; Lavender, W. M.; Plag, P. W.; King, A. S.; Kropf, A. J.; Bunker, B. A.; Kemner, K. M.; Dutta, P.; Duran, R. S.; Kaduk, J. The MR-CAT Insertion Device Beamline at the Advanced Photon Source. In *Synchrotron Radiation Instrumentation: Eleventh U.S. National Conference*; Pianetta, P., et al., Eds.; American Institute of Physics: New York, 2000; Vol. CP521, pp 419–422.
- (19) Kemner, K. M.; Kropf, J.; Bunker, B. A. A Low-Temperature Total Electron Yield Detector for X-ray Absorption Fine Structure Spectra. *Rev. Sci. Instrum.* **1994**, *65*, 3667–3669.
- (20) Stern, E. A.; Newville, M.; Ravel, B.; Yacoby, Y.; Haskel, D. The UWXAFS Analysis Package: Philosophy and Details. *Phys. B* **1995**, *208* and *209*, 117–120.
- (21) Newville, M.; Li, viñš P.; Yacoby, Y.; Rehr, J. J.; Stern, E. A. Near-Edge X-ray-Absorption Fine Structure of Pb: A Comparison of Theory and Experiment. *Phys. Rev. B* **1993**, *47* (21), 14126–14131.
- (22) Newville, M.; Ravel, B.; Haskel, D.; Stern, E. A. Analysis of Multiple Scattering XAFS Data Using Theoretical Standards. *Phys. B* **1995**, *208* and *209*, 154–156.
- (23) Haskel, D.; Ravel, B.; Newville, M.; Stern, E. A. Single and Multiple Scattering Xafs in BaZrO<sub>3</sub>: A Comparison Between Theory and Experiment. *Phys. B* **1995**, *208* and *209*, 151–153.
- (24) Sevilano, E.; Meuth, H.; Rehr, J. J. Extended X-ray Absorption Fine Structure Debye–Waller Factors: I Monatomic Crystals. *Phys. Rev. B* **1979**, *20* (12), 4908.
- (25) Newville, M. feffit: Using feff to Model XAFS in R-space. Unpublished work, 1994. This documentation is part of the uwxafs3.0 package.
- (26) Stern, E. A.; Number of Relevant Independent Points in X-ray-Absorption Fine-Structure Spectra. *Phys. Rev. B* **1993**, *48* (13), 9825.
- (27) Gajt, S.; Clark, S. B.; Sutton, S. R.; Rivers, M. L. Smith, J. V. Synchrotron X-ray Microprobe Determination of Chromate Content Using X-ray Absorption Near-Edge Structure. *Anal. Chem.* **1993**, *65*, 1800.
- (28) Wyckoff, R. G. W. *Crystal Structures*; Interscience: New York, 1964; Vol. 1–6.
- (29) In the model for the Cr K-edge data, the degeneracy of the triangle-oxygen path is reduced because of the splitting of the Cr → O distances in the tetrahedral; therefore, it was not needed in the model for the Cr K-edge data.